ENHANCED ELECTROACTIVE ARTIFICIAL MUSCLE USING CNFS/IONIC LIQUID IN A PVDF(HFP) POLYMER GEL: A LOW-COST ALTERNATIVE TO CNT-BASED ACTUATORS

P. SALGADO-FIGUEROA [1], C. JULLIAN [1], J.D. MOZO [2], AND F. PAVEZ-CABEZAS [1]*

[1]*Departamento de Química Orgánica y Fisicoquímica, Facultad de Ciencias Químicas y Farmacéuticas, Universidad de Chile.*
[2]*CCTH, Centro Científico y Tecnológico de Huelva, Facultad de Ciencias Experimentales. Universidad de Huelva.*

ABSTRACT

This study presents the development and characterization of two electroactive actuators, ACT-L1 and ACT-L2, based on carbon nanofibers (CNFs) and two different ionic liquids: EMIBF4 (L1) and EMIN[(CN)2] (L2). The actuators were designed in a three-layer configuration and characterized using SEM, AFM, FT-IR, IEC, and Young's modulus analysis.

SEM and AFM images revealed that electrode layers with L2 exhibited spherical grains and increased roughness, while FT-IR confirmed modifications in the polymer's crystalline structure due to CNFs and ionic liquid incorporation. The electrolyte films exhibited similar chemical and mechanical properties regardless of the ionic liquid used, except for roughness.

Performance evaluation demonstrated that both actuators showed stable and reproducible movement under a ±2.0 V voltage window. However, ACT-L1 achieved a maximum displacement of 400 µm, significantly outperforming ACT-L2 (17 µm), likely due to morphological differences in the electrolyte surface. The strain generated by ACT-L1 under ±2.0 V and 0.1 Hz was comparable to previously reported multiwalled carbon nanotube (MWCNT) actuators.

These results suggest that CNF-based actuators offer a promising and cost-effective alternative to CNT-based artificial muscles for applications in robotics, biomedical devices, and other fields.

Keywords: Electroactive Artificial Muscle, Electrochemical Actuator, Carbon Nanofiber (CNFs), PVdF(HFP) Polymer, Ionic Liquid, Electroactive Polymers.

1. INTRODUCTION

Electromechanical actuators, also known as artificial muscles, play a crucial role in applications such as robotics, mechatronics, and biomedical engineering [1,2]. Various materials have been explored for actuator fabrication, including carbon nanotube (CNT) sheets [3], electroactive polymers blended with ionic liquids [4], graphene-polystyrene composites [5,6] and electrochemically powered CNT [7]. Among these, CNT-based actuators have shown remarkable performance, particularly when blended with ionic liquids (ILs) [8-15].

Carbon nanofibers (CNFs) have emerged as a promising alternative to CNTs due to their semiconducting properties, high surface area, and chemical reactivity [16,17]. Unlike CNTs, CNFs offer a more cost-effective and scalable option for electroactive applications. They have been widely used as catalyst supports [17], reinforcing agents in polymer composites [18], and energy storage materials for supercapacitors [8].

Ionic liquids (ILs) have gained attention for their unique chemical and physical properties, making them ideal electrolytes for electrochemical actuators. ILs enhance conductivity and ionic transport in polymer matrices and have been successfully employed in electropolymerization, electrodeposition, and electrochemical devices such as batteries and semiconductors [19,20].

Fluoropolymers, such as polyvinylidene fluoride (PVdF) and polyvinylidene fluoride-co-hexafluoropropylene (PVdF(HFP)), are among the most commonly used electroactive polymers due to their excellent mechanical strength, thermal stability, and biocompatibility [21-24]. PVdF-based actuators, combined with ILs, have demonstrated efficient performance in bending motion applications [25-28].

Actuators are essential for converting energy into motion, with applications ranging from macroscopic robotics to microscale surgical instruments [29]. Natural actuators, such as muscles, function through electrochemical mechanisms, whereas artificial actuators rely on pneumatic, piezoelectric, ferroelectric, or electrochemical processes [30]. Electrochemical actuators, in particular, have gained prominence due to their ability to generate mechanical displacement with low weight, fast response times, and long cycle life [16,31].

Despite their advantages, CNT-based actuators face challenges due to the high cost of CNT synthesis, which limits their large-scale application. CNFs provide a cost-effective alternative, offering comparable electrical conductivity while maintaining desirable mechanical properties [32-34].

Most reported actuators employ a three-layer sandwich configuration, where ILs are incorporated into the electrode and electrolyte layers. In this work, we propose the development of CNF-based artificial muscles, leveraging the availability and affordability of CNFs as an alternative to CNTs. Our approach integrates CNFs, PVdF(HFP), and ILs into a three-layer configuration, with CNFs-IL-polymer as the electrode layer and PVdF(HFP)-IL as the electrolyte layer. We investigate the individual characterization of each layer, the influence of different ILs on actuator performance, and the actuator's efficiency in open-air conditions.

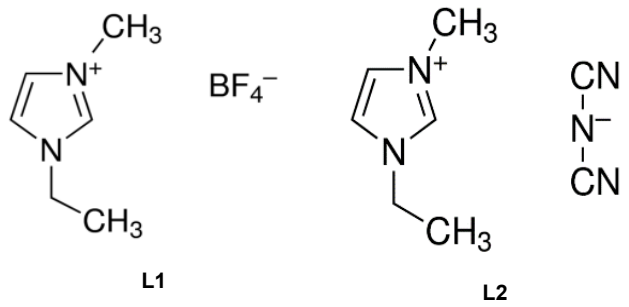

Figure 1: Chemical structure of L1: 1-Ethyl-3-methylimidazolium tetrafluoroborate ($EMIBF_4$) and L2: 1-Ethyl-3-methylimidazolium dicyanamide ($EMIN[(CN)_2]$).

2. EXPERIMENTAL

2.1 Reagents and materials.

Carbon nanofibers were provided by Dropsens. The ionic liquids (ILs) 1-Ethyl-3-methylimidazolium tetrafluoroborate (EMIBF4) and 1-Ethyl-3-methylimidazolium dicyanamide (EMIN[CN]2), referred to as L1 and L2, respectively, were obtained from Sigma Aldrich. Additional reagents, including N,N-dimethylacetamide (DMAC), 4-Methyl-2-pentanone (MP), and polyvinylidene fluoride-co-hexafluoropropylene (PVdF(HFP)), were also supplied by Sigma Aldrich and used without further purification. Propylene carbonate (PC) was purchased from Fluka, while succinic acid (EMSURE®) and sodium hydroxide pellets were obtained from Merck.

2.2 Fabrication of electrode and electrolyte layers.

o prepare the CNFs-IL-polymer suspensions, 50 mg of CNFs, 120 mg of L1 or L2, and 80 mg of PVdF(HFP) were combined in a 20 mL glass vial. After adding 9 mL of DMAc, the mixture was sonicated for 8 hours in an ultrasonic bath to ensure homogeneous dispersion. A 1.6 mL aliquot of this suspension was cast

**Corresponding author email: psalgado@ciq.uchile.cl*

into a Teflon mold (circular, 2.5 cm diameter) and left to dry at 70°C overnight. The final composition was 20 wt% CNFs, 48 wt% L1 or L2, and 32 wt% PVdF(HFP). These electrode layers are referred to as EE-L1 and EE-L2.

For the electrolyte gel layer, a solution was prepared by dissolving 400 mg of L1 or L2 and 400 mg of PVdF(HFP) (0.5 mmol/100 mg) in 4 mL of MP and 1000 mg of PC. The mixture was sonicated for 8 hours to ensure uniformity. Subsequently, 0.3 mL of the solution was cast into a Teflon mold (circular, 2.5 cm diameter) and dried at 70°C overnight to form the electrolyte layer. These layers are referred to as EY-L1 and EY-L2.

2.3 Actuator.

The actuator was fabricated in a sandwich configuration, consisting of two electrode layers and one electrolyte gel layer, all containing the same ionic liquid (L1 or L2), as shown in Figure 2. The layers were assembled using hot pressing at 26 lb and 70°C for 60 seconds with a custom-built hot press. Two actuators were obtained: ACT-L1, incorporating L1, and ACT-L2, incorporating L2.

The thickness of the fabricated electrode and electrolyte films, as well as the final actuator, was measured at five different positions (left, right, center, upper, and lower side) using a micrometer, optical microscope, and scanning electron microscopy (SEM) to ensure consistency and uniformity.

Figure 2: Schematic representation of the sandwich configuration of the CNFs actuator, composed of two electrode layers and one electrolyte layer.

2.4 Characterization of the polymer-supported electrode and electrolyte.

2.4.1 SEM images.

High-resolution scanning electron microscopy (HR-SEM) was performed using an INSPECT-F50 (SEI) and a Phenom ProX desktop SEM. Images were captured at multiple magnifications from a 10×10 mm² section of the carbon nanofiber electrode and electrolyte layers. To enhance imaging contrast, each sample was coated with a thin gold layer before SEM observation.

2.4.2 AFM images.

Atomic force microscopy (AFM) was conducted using a Digital Nanoscope III to examine the surface morphology of the electrode and electrolyte films. The acquired AFM images were processed and analyzed using Gwyddion, a specialized software for scanning probe microscopy.

2.4.4 ATR-FTIR.

Fourier-transform infrared spectroscopy (FT-IR) in Attenuated Total Reflection (ATR) mode was performed using a Thermo Scientific iS50 FT-IR spectrometer to investigate the chemical interactions within the electrode and electrolyte films.

2.4.5 Ion exchange capacity (IEC).

To determine the ionic exchange capacity (IEC), electrode and electrolyte films (4.91 cm²) were prepared in circular Teflon molds. Each film was immersed in 2 M HCl for 24 hours to facilitate H^+ ion exchange, followed by immersion in 2 M NaCl for 24 hours to replace H^+ with Na^+ cations. Films were then rinsed with deionized water before IEC determination through titration with 0.01 M NaOH, as calculated using Equation (1):

$$IEC = \frac{x \times M_{NaOH}}{W_{Film}} \qquad \text{Equation (1)}$$

Where **x** is the volume of NaOH (mL) used, $\mathbf{M_{NaOH}}$ is its molarity and $\mathbf{W_{Film}}$ is the dry weight of the film.

2.4.6 Tensile properties.

The mechanical properties of the films were assessed using a Lloyd TA-1 material testing machine, following the ASTM D882 standard. Strips (10 × 1.2 cm²) were prepared for both the CNF-based electrodes and electrolyte films. Young's modulus was calculated from stress-strain curves, with tests conducted at room temperature and a loading rate of 1.0 mm/min.

2.4.7 Displacement measurement.

Chronoamperometry was performed on a 10 mm × 1 mm actuator strip in an open-air configuration at 0.1 Hz, applying a cyclic voltage of -2 V to +2 V. Additional tests were carried out at varying frequencies (0.05 to 1.0 Hz) and voltage windows (± 0.5 to ± 4.0 V) using a Metrohm Autolab AUT86461 potentiostat/galvanostat. The displacement (δ) was tracked in real time with a laser displacement meter (MTI Instruments) and a CCD camera, monitoring a fixed point 6 mm from the anchored end to evaluate the actuator's bending motion.

3. RESULTS AND DISCUSSION

Two CNFs gel/IL-polymer actuators (ACT-L1 and ACT-L2) were fabricated in a three-layer configuration, consisting of a polymer gel/IL electrolyte layer (EY-L1, EY-L2) sandwiched between two CNFs/IL-polymer electrode layers (EE-L1, EE-L2), as shown in Figure 2.

The surface morphology of these layers (EE-L1, EE-L2, EY-L1, and EY-L2) was analyzed using SEM at magnifications ranging from 1kX to 20kX. SEM imaging of EY-L2 proved challenging due to the high accelerating voltage (15 kV) required, even with gold sputter coating to minimize charging effects. To address this, FESEM was used at a lower accelerating voltage (0.5 kV, 3.5kX magnification) to obtain clearer images.

A Phenom ProX desktop SEM was additionally employed to characterize CNF-based electrode films without the need for gold sputter coating. As shown in Figures 3 and 4, both EE-L1 and EE-L2 exhibited a smooth and uniform surface morphology (SEM 15 kV, 500kX), indicating that the incorporation of CNFs and ILs did not significantly alter the homogeneity of the polymer matrix. This suggests that the CNFs and ILs are well dispersed within the polymer, ensuring consistent electrochemical performance and mechanical integrity.

A detailed examination of the surfaces of EE-L1 and EE-L2 (Figures 3 and 4, insets a-b) reveals that their morphology depends on the ionic liquid used during electrode preparation. In the case of L1, amorphous grains with homogeneously distributed pores were observed, whereas L2 exhibited spherical grains with significantly reduced porosity. The formation of these pores is attributed to solvent evaporation during film formation, which may influence ionic conductivity and mechanical properties.

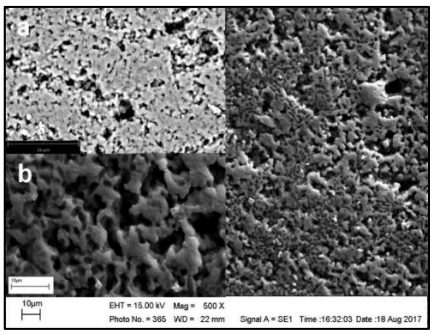

Figure 3: SEM images of the surface morphology of EE-L1 at 500× magnification. Inset (a): Phenom ProX SEM at 4k×. Inset (b): SEM at 2k×.

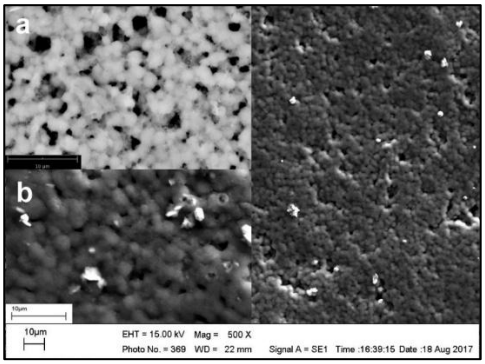

Figure 4: SEM images of the surface morphology of EE-L2 at 500× magnification. Inset (a): Phenom ProX SEM at 7k×. Inset (b): SEM at 2k×.

Regarding the presence of spherical grains in EE-L2, previous studies have reported similar observations. Zhao et al. [35] identified spherical particles on PVdF/MWCNT composites using FESEM imaging, while Jin et al. [36] and Zhang et al. [37] described comparable morphologies in PVdF/CNT and PP/CNT composites, respectively. This phenomenon has been linked to the interaction between MWCNTs and PVdF induced by ultrasonic cavitation during the sonication process. Similarly, composites incorporating ionic liquids, carbon nanotubes, and polymers often exhibit an amorphous surface morphology [9, 22, 23]. Our findings align with this trend for CNFs/PVdF(HFP)/L1, whereas the presence of L2 resulted in spherical particle formation (Figure 5). These observations suggest that the interaction between L2, CNFs, and PVdF(HFP) likely promotes spherical particle formation, rather than CNFs alone being responsible for this behavior. The precise mechanism for this phenomenon remains unclear; however, the difference between the two layers is the counterion of 1-Ethyl-3-methylimidazolium, which we hypothesize plays a key role in the formation of spherical particles in the presence of CNFs.

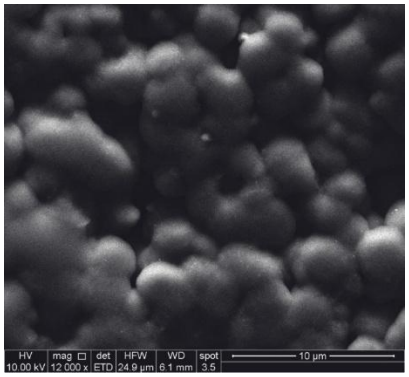

Figure 5: FESEM image of spherical particles observed on the EE-L2 surface at 12k× and 10 kV.

Figures 6a and 6b (FESEM, 0.5 kV, 4k×) present the SEM micrographs of EY-L1 and EY-L2, revealing a smooth and uniform surface morphology. These observations indicate good compatibility between the polymer and the ionic liquid, independent of the IL species used in the formation of PVdF(HFP) films.

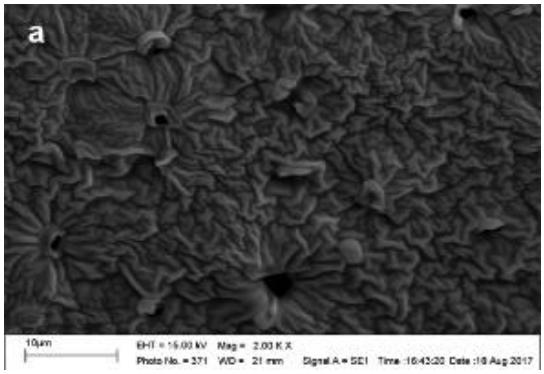

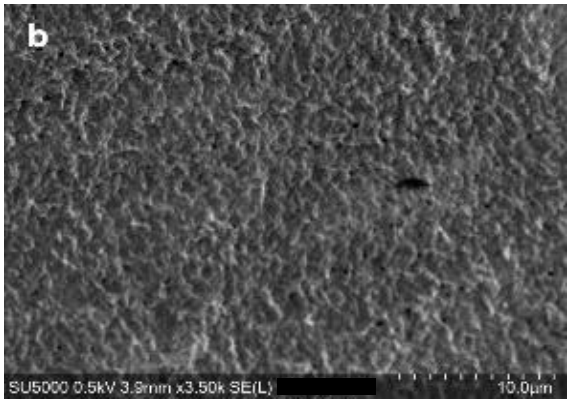

Figure 6: SEM images of the electrolyte layers. (a) EY-L1 at 2k× magnification. (b) EY-L2 at FESEM 4k×.

The two- and three-dimensional surface topography of the CNF-based electrode and electrolyte layers was further analyzed using AFM. The scanning areas were 50 × 50 µm² for the electrodes and 12.5 × 12.5 µm² for the electrolyte layers. 2D micrographs confirm that both surfaces are smooth, with some polymer aggregates detected. EDS analysis identified these aggregates as undissolved polymer residues.

Grain size analysis performed using Gwyddion software revealed that EE-L1 and EE-L2 have average dimensions of 1.7 ± 0.2 µm × 0.20 ± 0.01 µm and 3.1 ± 0.4 µm × 0.32 ± 0.03 µm, respectively. These values are consistent with those obtained from SEM micrographs (2.2 ± 0.2 µm and 3.4 ± 0.4 µm). Roughness analysis indicated that EY-L1 exhibited lower roughness than EY-L2, while both electrolyte layers were rougher than the electrode layers (EE-L1 and EE-L2). The correlation between roughness and grain size suggests that larger grain structures in EE-L2 and EY-L2 contribute to increased surface roughness, which may influence ionic transport and mechanical properties (Table 1).

FTIR-ATR is a powerful tool to study structural changes, the nature of bonds, and interactions among the constituents of electrode CNFs-polymer films. The FTIR spectra for pure PVdF(HFP), EE-L1, and EE-L2 are shown in Figure 7. PVdF(HFP) is a semi-crystalline polymer where vinylidene fluoride (VdF) forms the crystalline phase, and hexafluoropropylene (HFP) forms the amorphous phase. The amorphous phase of PVdF(HFP) assists in trapping a high quantity of electrolytes, whereas the crystalline phase acts as mechanical support for the film [22] The crystalline phase, or the α phase [23] of pure PVdF(HFP) is identified by vibrational bands at 976 cm^{-1}, 763 cm^{-1}, and 608 cm^{-1}, while the amorphous phase, or β phase [24] is confirmed by the presence of vibrational bands at 873 cm^{-1} and 839 cm^{-1}. In the case of EE-L1 and EE-L2, the vibrational bands corresponding to the β phase are notably different from pure PVdF(HFP), as the band at 873 cm^{-1} shifts to 879 cm^{-1}, and the peak at 839 cm^{-1} becomes prominent. Additionally, the peak of the crystalline phase at 976 cm^{-1} disappears, and the peak at 608 cm^{-1} shifts to 620 cm^{-1} in both EE-L1 and EE-L2. These results indicate that the crystalline structure of the polymer was modified by the presence of CNFs and ionic liquid, resulting in a more amorphous structure in both electrode films.

The remaining FTIR bands in all three films show no significant shifts. For instance, the 1430 cm^{-1} band corresponds to >C-O-C< stretching vibrations, while the 1402 cm^{-1} peak is associated with C-O stretching from the plasticizer [38]. The 1230 cm^{-1} peak is linked to the γ-phase of PVdF(HFP). However, some shifts were observed at 1180 cm^{-1} toward lower energy values. Additionally, the -C-F- stretching band at 1280 cm^{-1} shifts to 1267 cm^{-1}, while the -CF_2- stretching band at 1180 cm^{-1} shifts to 1173 cm^{-1} for both EE-L1 and EE-L2.

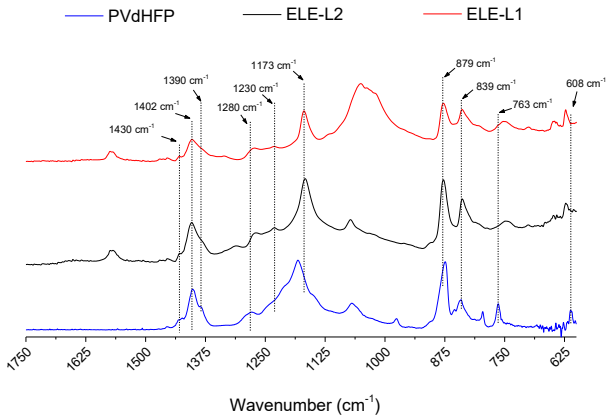

Figure 7: FTIR-ATR spectra of pure PVdF(HFP), EE-L1, and EE-L2.

The ionic exchange capacity (IEC) was determined by a titration method using 0.01 M NaOH with phenolphthalein as an indicator and calculated according to Equation 1. The IEC values obtained were similar for both electrode and electrolyte films: EE-L1 (0.34 meq/g), EE-L2 (0.36 meq/g), EY-L1 (0.31 meq/g), and EY-L2 (0.32 meq/g), despite differences in composition (32 wt% and 50 wt% of PVdF(HFP) for EE and EY, respectively).

Although the electrolyte film contains a higher polymer concentration and lacks CNFs, its IEC values remain comparable to those of the electrode films. This can be attributed to the amorphous phase of PVdF(HFP), which enhances electrolyte retention, promoting ion exchange. The incorporation of CNFs into the electrode film further modifies the crystalline phase, leading to a more amorphous structure and increased porosity, which facilitates ion transport.

Terasawa et al. [39] proposed that the bending motion mechanism in actuators occurs due to the migration of cations and anions within the gel electrolyte layer, where cations move toward the cathode and anions toward the anode upon voltage application. Since both electrode and electrolyte layers exhibit similar IEC values, this would enable efficient cation transport across intra- and interlayer interfaces, enhancing the overall performance of the actuator.

A mechanical test was conducted on the electrode and electrolyte layers at a loading rate of 1 mm/min using a Lloyd material testing machine, obtaining stress-strain curves and Young's modulus values. Since electrode stiffness is a key parameter in actuator response and power, the Young's modulus of each layer was analyzed (Table 1). The results showed that the electrode layers exhibited higher stiffness than the electrolyte layers, which can be attributed to the incorporation of CNFs, reducing the degree of crystallinity in the polymer.

Table 1

Layer	Thickness (µm)	Roughness (nm)	Young´s modulus (MPa)	ε_B (%)	σ_B (MPa)	IEC (meq/g)
EE-L1	88± 3	51 ± 6	127 ± 5	36 ± 7	3,5 ± 0,2	0,34 ± 0,01
EE-L2	98± 9	43 ± 7	76 ± 1	46 ± 5	2,2 ± 0,1	0,36 ±0,06
EY-L1	42± 3	54 ± 8	43 ± 4	82 ± 8	3,5 ± 0,1	0,31 ± 0,03
EY-L2	38± 4	103 ± 16	40 ± 1	83 ± 7	3,2 ± 0,2	0,32 ± 0,01

Among the electrode layers, EE-L1 (127 MPa) had a higher modulus than EE-L2 (76 MPa). The lower modulus of EE-L2 may be due to its spherical particle morphology, which could increase elasticity compared to EE-L1. Comparing our CNF-based electrodes with SWCNT-based electrodes prepared by Terasawa et al., both using the same ionic liquid (EMIBF4), we find that CNF-based electrodes exhibit a lower Young's modulus (127 MPa vs. 141 MPa for SWCNTs) [11]. This suggests that CNFs provide greater elasticity, which could be advantageous for applications requiring flexibility in actuators.

The electrolyte layers (EY-L1 and EY-L2) exhibited similar mechanical properties, independent of the IL species, with Young's modulus values of 43 MPa and 40 MPa, respectively. However, roughness analysis revealed that EY-L2 exhibited twice the roughness of EY-L1, which can be correlated with the presence of spherical particles observed in SEM micrographs. Tensile strength (σB) values of 3.5 MPa (EY-L1) and 3.2 MPa (EY-L2) were lower than those reported for electrospun PVdF(HFP) fibers (5.6 MPa) [29], confirming a reduction in crystallinity in the electrolyte films.

Following the characterization of individual layers, the complete ACT-L1 and ACT-L2 actuators were fabricated using a sandwiched configuration, consisting of two electrode layers (EE-L1 or EE-L2) and one electrolyte layer (EY-L1 or EY-L2), sharing the same IL species. The final thickness of the actuators was 180–190 µm, slightly lower than the expected 214–238 µm, likely due to pressure and heat applied during the hot-pressing process.

Chronoamperometry was used to analyze the displacement (δ) performance in open air and to determine the optimal frequency and voltage window. First, a voltage cycle of ±2.0 V was applied at different frequencies (0.05–1.0 Hz) to an ACT-L1 strip (10 mm × 1 mm) in a two-electrode configuration. The displacement was monitored at 6 mm from a fixed point using a laser displacement meter (MTI Instruments) and a CCD camera. The actuators exhibited greater displacement at lower frequencies (0.05 and 0.1 Hz). The best performance was observed at 0.1 Hz, which was selected as the working frequency, balancing actuator response time and efficiency.

Next, different voltage windows (±0.5 to ±4.0 V) were applied at 0.1 Hz to evaluate the optimal voltage window. The measured displacement (δ) was converted into strain (ε) using Equation 2:

$$\varepsilon = \frac{2d\delta}{L^2+\delta^2} \qquad \text{Equation (2)}$$

where L is the free length, δ is the displacement, and d is the actuator thickness, assuming no thickness variation during bending [17].

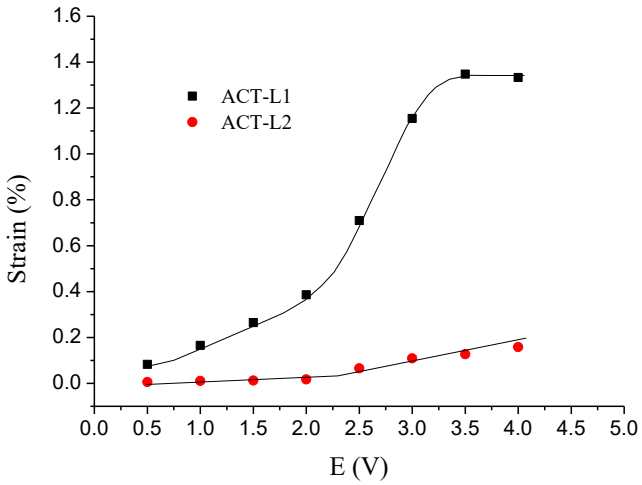

Figure 8: Dependence of generated strain on applied voltage at a frequency of 0.1 Hz.

Figure 8 illustrates the strain generated in ACT-L1 and ACT-L2 as a function of applied voltage at 0.1 Hz. ACT-L2 exhibited a slight increase in strain across all voltage ranges. In contrast, ACT-L1 showed a continuous strain increase from 0.5 V to 3.5 V, maintaining a plateau beyond 3.5 V. As voltage increased, strain also increased, reaching 0.39% at 0.1 Hz and 2.0 V, comparable to the MWCNT-COOH/EMI[BF4] actuator reported by Terasawa et al. (0.32–0.44% at 2.0 V) [40]. These results suggest that ACT-L1 can generate strain levels similar to MWCNT-based actuators, making it a potential candidate for robotics and other applications.

To assess actuator durability, a lifetime study was conducted at 0.1 Hz and ±2.0 V, followed by tests at higher voltages that had previously resulted in greater displacement (±3.5 V for ACT-L1 and ±4.0 V for ACT-L2). ACT-L1 maintained reproducible bending motion for 7 hours, after which its displacement slightly decreased but remained stable until 27 hours. At 28 hours, its performance significantly declined. Similarly, ACT-L2 exhibited stable behavior at ±2.0 V, with a lifetime of 23.2 hours. However, its performance deteriorated drastically when ±4.0 V was applied, reducing its operational time to just 0.3 hours. At higher voltages, both actuators experienced rapid performance degradation, confirming that ±2.0 V is the optimal voltage window for sustained operation.

During actuation, visual inspection did not reveal significant damage. However, SEM analysis showed delamination and edge cracking (Figure 9). These findings suggest that layer adhesion is a critical factor for efficient ion transport across intra- and interlayers, directly impacting actuator longevity. This aligns with observations reported by Terasawa et al., who emphasized that strong adhesion between layers is essential for achieving rapid and reproducible actuation [41].

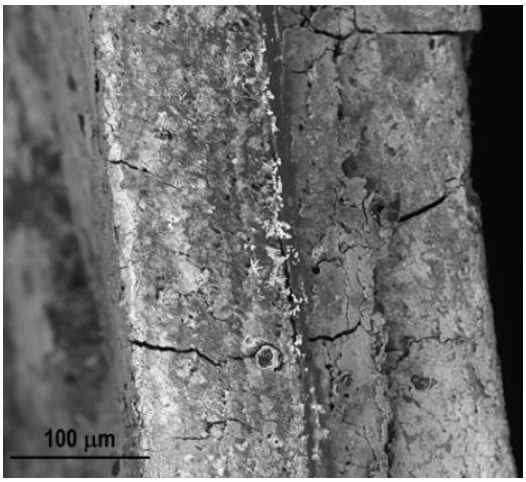

Figure 9: SEM image of ACT-L1 after its cycle-life test, at 740× magnification and 10 kV.

CONCLUSION

In this study, two actuators (ACT-L1 and ACT-L2) were successfully fabricated using carbon nanofibers (CNFs), polymer, and two different ionic liquids (L1 and L2) in a sandwiched configuration. The chemical and mechanical properties of each actuator layer were extensively characterized. FTIR analysis confirmed that the incorporation of CNFs and ionic liquids altered the polymer's crystalline structure, promoting a more amorphous configuration in both electrode films. SEM and AFM imaging revealed significant differences in surface morphology between electrode layers prepared with L1 and L2, with L2-based films exhibiting a spherical grain morphology with higher roughness. Additionally, L2-based films demonstrated a lower Young's modulus, higher elongation at break, and greater elasticity compared to those prepared with L1. While electrolyte layers exhibited similar Young's modulus values, EY-L2 displayed higher roughness than EY-L1. Despite these variations, SEM micrographs confirmed a smooth and uniform morphology for both electrode and electrolyte films, suggesting good compatibility between CNFs/polymer/ionic liquid and polymer/ionic liquid systems.

When actuated at ±2.0 V and 0.1 Hz, ACT-L1 outperformed ACT-L2, despite the greater elasticity and roughness of ACT-L2, which would typically enhance ion transport and mechanical flexibility. However, the spherical particle morphology observed in ACT-L2 films may have counteracted this effect, limiting efficiency during bending motion. These findings suggest that morphological analysis via SEM or AFM could serve as a predictive tool for assessing actuator feasibility before assembly.

The generated strain (0.39%) for ACT-L1 at ±2.0 V and 0.1 Hz was comparable to MWCNT actuators (0.32%) reported in previous studies using the same ionic liquid [40]. This indicates that CNF-based actuators can generate sufficient strain, similar to MWCNT actuators, while offering a low-cost alternative. Furthermore, ACT-L1 exhibited reproducible and stable bending motion in open air, with a long operational lifetime of 28 hours. These results confirm that CNFs are a promising material for low-cost artificial muscles in a three-layer configuration, with potential applications in robotics, biomedical devices, and other fields.

ACKNOWLEDGMENT

This work was supported by Fondecyt project No. 11140392. Thanks to Melvyn Becerra & Cía. Ltda. for providing the Phenom ProX desktop SEM images.

REFERENCES

1. Vohrer, U.; Kolaric, I.; Haque, M. H.; Roth, S.; (Sobhan Sharafkhani, 2021) Detlaff-Weglikowska, U. Carbon N. Y, 2004, 42, 1159–1164, doi:10.1016/j.carbon.2003.12.044.
2. Mahanty, B.; Maity, K.; Sarkar, S.; Mandal, D. Mater. Today Proc. 2020, 21, 1964–1968, doi:10.1016/j.matpr.2020.01.282.
3. Fraysse, J.; Minett, A. I.; Jaschinski, O.; Duesberg, G. S.; Roth, S. Carbon N. Y. 2002, 40, 1735–1739, doi:10.1016/S0008-6223(02)00041-6.
4. Kwon, K. S.; Ng, T. N. Org. Electron. physics, Mater. Appl. 2014, 15, 294–298, doi:10.1016/j.orgel.2013.11.026.
5. Lee, B. K.; Park, S. J.; Kim, D. S. Curr. Appl. Phys. 2013, 13, 1520–1524, doi:10.1016/j.cap.2013.05.011.
6. Prasad, B.; Gill, F. S.; Panwar, V.; Anoop, G. Compos. Part B Eng. 2019, 173, 106990, doi:10.1016/j.compositesb.2019.106990.
7. Park C-L.; Goh B.; Kim E.; Choi J.; Kim S., Carbon, Volume 220, 20 February 2024, 118775, https://doi.org/10.1016/j.carbon.2023.118775
8. Terasawa, N.; Ono, N.; Mukai, K.; Koga, T.; Higashi, N.; Asaka, K. Carbon N. Y. 2012, 50, 311–320, doi:10.1016/j.carbon.2011.08.072.
9. Chen, I.-W. P.; Cottinet, P.-J.; Tsai, S.-Y.; Foster, B.; Liang, R.; Wang, B.; Zhang, C. Sensors Actuators B Chem. 2012, 171–172, 515–521, doi:10.1016/j.snb.2012.05.022.
10. Takeuchi, I.; Asaka, K.; Kiyohara, K.; Sugino, T.; Terasawa, N.; Mukai, K.; Fukushima, T.; Aida, T. Electrochim. Acta, 2009, 54, 1762–1768, doi:10.1016/j.electacta.2008.10.007.
11. Biso, M.; Ansaldo, A.; Picardo, E.; Ricci, D. Carbon N. Y., 2012, 50, 4506–4511, doi:10.1016/j.carbon.2012.05.032.
12. Terasawa, N.; Takeuchi, I.; Matsumoto, H. Sensors Actuators, B Chem. 2009, 139, 624–630, doi:10.1016/j.snb.2009.03.057.
13. Mukai, K.; Asaka, K.; Kiyohara, K.; Sugino, T.; Takeuchi, I.; Fukushima, T.; Aida, T. Electrochim. Acta, 2008, 53, 5555–5562, doi:10.1016/j.electacta.2008.02.113.
14. Sugino, T.; Kiyohara, K.; Takeuchi, I.; Mukai, K.; Asaka, K. Sensors Actuators, B Chem. 2009, 141, 179–186, doi:10.1016/j.snb.2009.06.002.
15. Sobhan Sharafkhani, M, K 2021, 10 (9060).
16. Terasawa, N.; Takeuchi, I. Electrochim. Acta, 2014, 123, 340–345, doi:10.1016/j.electacta.2013.12.156.
17. Jung, J. H.; Vadahanambi, S.; Oh, I. K. Compos. Sci. Technol, 2010, 70, 584–592, doi:10.1016/j.compscitech.2009.12.007.
18. Jung, J. H.; Jeon, J. H.; Sridhar, V.; Oh, I. K. Carbon N. Y. 2011, 49, 1279–1289, doi:10.1016/j.carbon, 2010, 11.047.
19. Łuczak, J.; Hupka, J.; Thöming, J.; Jungnickel, C. Colloids Surfaces A Physicochem. Eng. Asp. 2008, 329, 125–133, doi:10.1016/j.colsurfa.2008.07.012.
20. Shiddiky, M. J. A.; Torriero, A. A. J. Biosens. Bioelectron. 2011, 26, 1775–1787, doi:10.1016/j.bios.2010.08.064.
21. Yuan, C.; Su, L.; Yang, K.; Li, Z.; Cheng, X.; Wang, Y.; Li, L. Colloid Polym. Sci. 2015, 293, 925–932, doi:10.1007/s00396-014-3466-7.
22. Wu, Y. S.; Yang, C. C.; Luo, S. P.; Chen, Y. L.; Wei, C. N.; Lue, S. J. Int. J. Hydrogen Energy 2017, 42, 6862–6875, doi:10.1016/j.ijhydene.2016.11.201.
23. Daneshkhah, A.; Shrestha, S.; Agarwal, M.; Varahramyan, K. Sensors Actuators, B Chem. 2015, 221, 635–643, doi:10.1016/j.snb.2015.06.145.
24. Kabir, E.; Khatun, M.; Nasrin, L.; Raihan, M. J.; Rahman, M. J. Phys. D. Appl. Phys., doi:10.1088/1361-6463/aa5f85.
25. Gong W.; Yang W.; Fu F.; Nano Energy 131, 2024, 110277
26. Wu, C. G.; Lu, M. I.; Chuang, H. J. Polymer (Guildf). 2005, 46, 5929–5938, doi:10.1016/j.polymer.2005.05.077.
27. Wang, J.; Zheng, L.; Wu, Z.; Zhang, Y.; Zhang, X. J. Memb. Sci. 2016, 497, 183–193, doi:10.1016/j.memsci.2015.09.024.
28. Sil, A.; Sharma, R.; Ray, S. Surf. Coatings Technol. 2015, 271, 201–206, doi:10.1016/j.surfcoat.2014.12.036.
29. Minett, A.; Fràysse, J.; Gang, G.; Kim, G.-T.; Roth, S. Curr. Appl. Phys. 2002, 2, 61–64, doi:10.1016/S1567-1739(01)00100-6.
30. Canning, J.; Bandyopadhyay, S.; Biswas, P.; Aslund, M. World ' s largest Science , Technology & Medicine Open Access book publisher., doi:10.5772/50570.
31. Spasova, M.; Manolova, N.; Markova, N.; Rashkov, I. Appl. Surf. Sci. 2016, 363, 363–371, doi:10.1016/j.apsusc.2015.12.049.
32. Soroush Soltani, N, K 2022, 12 (6111).
33. Hong Huang, Biyun Chen, Jun Wu, Yuan Wang, Zhangfeng Shen, Lifen Li, Yan Wang, Yangang Wang, Xi Li. Materials Today Communications, 2022, 103052, https://doi.org/10.1016/j.mtcomm.2021.103052
34. Keshavarz S.; Okoro O.; Hamidi M., Coordination Chemistry Reviews, Volume 472, 2022, 214770, https://doi.org/10.1016/j.ccr.2022.214770.

35. Zhao, Z.; Zheng, W.; Yu, W.; Long, B. Carbon N. Y. 2009, 47, 2118–2120, doi:10.1016/j.carbon.2009.03.043.
36. Jin, Z.; Pramoda, K. P.; Goh, S. H.; Xu, G. Composites. Mater. Res. Bull. 2002, 37, 271–278, doi:10.1016/S0025-5408(01)00775-9.
37. Zhang, S.; Kumar, S. . Macromol. Rapid Commun. 2008, 29, 557–561.
38.Saikia, D.; Kumar, A. I, Electrochim. Acta 2004, 49, 2581–2589, doi:10.1016/j.electacta.2004.01.029.
39. Terasawa, N.; Ono, N.; Hayakawa, Y.; Mukai, K.; Koga, T.; Higashi, N.; Asaka, K. Sensors Actuators, B Chem. 2011, 160, 161–167, doi:10.1016/j.snb.2011.07.027.
40. Terasawa, N.; Ono, N.; Mukai, K.; Koga, T.; Higashi, N.; Asaka, K. Sensors Actuators, B Chem. 2012, 163, 20–28, doi:10.1016/j.snb.2011.11.065.
41.Terasawa, N.; Asaka, K. RSC Adv. 2016, 6, 66360–66367, doi:10.1039/C6RA08676D.